Chinese Chemical Letters 37 (2026) 110414

Contents lists available at ScienceDirect

Chinese Chemical Letters

journal homepage: www.elsevier.com/locate/cclet

A MOF derived multi-phase $FeNi_3$-S catalyst for efficient hydrogen storage in magnesium hydride

Linxin Zheng[a,1], Shuai Li[a,1], Liuting Zhang[a,*], Tao Zhong[a], Xiuzhen Wang[a,*], Ting Bian[a], Petr Senin[c], Ying Wu[b,*]

[a] School of Energy and Power, Jiangsu University of Science and Technology, Zhenjiang 212003, China
[b] Institute of Energy Power Innovation, North China Electric Power University, Beijing 102206, China
[c] Institute of Mechanics and Power Engineering, Ogarev Mordovia State University, Saransk 430005, Russia

ARTICLE INFO

Article history:
Received 3 June 2024
Revised 1 September 2024
Accepted 5 September 2024
Available online 6 September 2024

Keywords:
Hydrogen storage
Magnesium hydride
Muti-phase catalysis
Kinetics
Reversibility

ABSTRACT

Magnesium hydride (MgH_2) demonstrates immense potential as a solid-state hydrogen storage material, while its commercial utilization is impeded by the elevated operating temperature and sluggish reaction kinetics. Herein, a MOF derived multi-phase $FeNi_3$-S catalyst was specially designed for efficient hydrogen storage in MgH_2. Experiments confirmed that the incorporation of $FeNi_3$-S into MgH_2 significantly lowered the desorption temperature and accelerated the kinetics of hydrogen desorption and reabsorption. The initial dehydrogenation temperature of the $MgH_2 + 10$ wt% $FeNi_3$-S composite was 202 °C, which was 123 °C lower than that of pure MgH_2. At 325 °C, the $MgH_2 + 10$ wt% $FeNi_3$-S composite released 6.57 wt% H_2 (fully dehydrogenated) within 1000 s. Remarkably, $MgH_2 + 10$ wt% $FeNi_3$-S composite initiated rehydrogenation at room temperature and rapidly absorbed 2.49 wt% H_2 within 30 min at 100 °C. Moreover, 6.3 wt% H_2 was still retained after 20 cycles at 300 °C, demonstrating the superior cycling performance of the $MgH_2 + 10$ wt% $FeNi_3$-S composite. The activation energy fitting calculations further evidenced the addition of $FeNi_3$-S enhanced the de/resorption kinetics of MgH_2 ($E_a = 98.6$ kJ/mol and 43.3 kJ/mol, respectively). Through phase and microstructural analysis, it was determined that the exceptional hydrogen storage performance of the composite was attributed to the *in-situ* formation of $Mg/Mg_2Ni + Fe/MgS$ and $MgH_2/Mg_2NiH_4 + Fe/MgS$ hydrogen storage systems. Further mechanistic analysis revealed that Mg_2Ni/Mg_2NiH_4 served as "hydrogen pump" and Fe/MgS served as "hydrogen diffusion channel", thus accelerating the dissociation and recombination of hydrogen molecules. In conclusion, this work offers insight into catalysts combining transition metal alloys and transition metal sulfide for exerting muti-phase synergistic effect on boosting the dehydrogenation/hydrogenation reactions of MgH_2, which can also inspire future pioneering work on designing and fabricating high efficient catalysts in other energy storage related areas.

© 2025 Published by Elsevier B.V. on behalf of Chinese Chemical Society and Institute of Materia Medica, Chinese Academy of Medical Sciences.

Increased energy consumption and depletion of fossil fuel reserves pose a hazard to global energy security and the economy [1]. In comparison to fossil fuels, hydrogen stands out as a promising alternative on account of its sustainability and eco-friendliness, while its low volumetric density under standard conditions is the primary impediment to the storage and transportation of hydrogen [2,3]. Over the past few decades, hydrogen storage methods including compressed hydrogen storage, liquid hydrogen storage, cryo-compressed hydrogen storage and solid hydrogen storage have got a spectacular development [4]. In terms of safety and efficiency, solid hydrogen storage comes to the fore, fueling a surge in research of solid-state materials for hydrogen storage [5]. Among miscellaneous materials, MgH_2 has been brought into sharp focus by its high volumetric (110 kg H_2/m^3) and gravimetric (7.6 wt% H_2) capacities, fantastic reversibility, and abundant magnesium reserves. Nevertheless, the high thermodynamic stability ($\Delta H = 76$ kJ/mol) and kinetic barrier ($E_a = 160$ kJ/mol), which bring about high-temperature desorption and sluggish hydrogen ab/desorption kinetics respectively, have hinder the practical application of MgH_2 in the long run [6,7].

In recent years, researchers have developed the following strategies to address the challenges: nanosizing the Mg particles [8–10], alloying Mg particles with mental elements [11–13] and

* Corresponding authors.
E-mail addresses: zhanglt89@just.edu.cn (L. Zhang), wangxiuzhenhome@163.com (X. Wang), wuying@ncepu.edu.cn (Y. Wu).
[1] These authors contributed equally to this work.

https://doi.org/10.1016/j.cclet.2024.110414
1001-8417/© 2025 Published by Elsevier B.V. on behalf of Chinese Chemical Society and Institute of Materia Medica, Chinese Academy of Medical Sciences.

adding different catalysts into Mg/MgH_2 hydrogen storage systems [14–16]. It has been proven that the addition of catalysts together with nanosized Mg particles *via* ball milling is the best bet to improve the performance of MgH_2 in both thermodynamic and kinetic aspects [17,18]. Transition metals (TM), such as Ni [19,20], Fe [21,22], Ti [23,24], Co [25,26], V [27,28], along with their alloys/compounds (oxides, sulfide, halides, hydrides *etc.*), exhibit significant catalytic effects on the kinetics of MgH_2. Some TMs like Ni and Co involve in the reaction and generate intermetallic hydrides of Mg_2NiH_4 and Mg_2CoH_5 *in situ*, thus serving as a "hydrogen pump" to accelerate the rates of hydrogen de/ab-sorption [29,30]. Apart from forming intermetallic hydrides, other TMs consist of Fe and Nb are also used as catalysts by virtue of the abundant d-orbital electron and excellent catalytic function [31]. Among all the TMs, M. Pozzo and his coworker have already proved that Ni and Fe (Ni ranks first) are the best possible choice to accelerate the kinetics of hydrogen absorption [32]. This work sheds light on the selection of transition metal elements. In addition, bimetallic catalysts have demonstrated higher efficiency than monometallic catalysts due to the synergistic effect [6,10]. Therefore, researchers have extensively investigated the effects of NiFe alloy catalysts on enhancing the hydrogen storage capabilities of MgH_2. Ding *et al.* synthesized a core-shell structural $Fe_{0.64}Ni_{0.36}$@C composite and observed that the initial desorption temperature of MgH_2-$Fe_{0.64}Ni_{0.36}$@C system was decreased to 250 °C. Besides, 5.18 wt% H_2 could be absorbed at 150 °C within 20 min [33]. Fu and coworkers found that NiFe@CNT decreased the onset desorption temperature of MgH_2 to 225 °C. Notably, the addition of NiFe@CNT significantly reduced the dehydrogenation activation energy of MgH_2 to 49.7 kJ/mol [31]. Both of Ding and Fu had reported the synergistic effect between Fe and in-suit formed $MgNi_2/Mg_2NiH_4$. Hence, the synergistic bimetallic catalysis of FeNi alloy has been confirmed to accelerate the reaction kinetics of MgH_2 and effectively lower the energy barrier of the reaction.

Recent studies have indicated that transition metal sulfides (TMS) possess excellent catalytic activity, which has been confirmed in the fields of hydrogen and oxygen evolution reactions [34,35]. Based upon these findings, it is of great significance to reveal whether transition metal sulfides can enhance the hydrogen storage properties of MgH_2. The research group led by Zhang had discovered that the addition of FeS_2 and Fe_3S_4 contributed positively to the enhancement of hydrogen storage behavior in MgH_2. They stated that the improved hydrogen storage capabilities of MgH_2 were attributed to the synergistic catalytic action between the Fe and *in-situ* formed MgS [36,37]. Zeng *et al.* introduced a Ni_3S_2@C catalyst into MgH_2 and found that the MgH_2–Ni_3S_2@C-4 composite was able to absorb 5.68 wt% H_2 upon dehydrogenation at 100 °C and release 6.35 wt% H_2 upon rehydrogenation at 275 °C [38]. Additionally, Fu and colleagues had also applied ternary transition metal catalysts to MgH_2. Under the synergistic catalysis of several active species, MgH_2-$FeNi_2S_4$ composite uptook 4.02 wt% H_2 at 100 °C for 1 h [16]. These finding underscored the potential of transition metal sulfides as additives for improving the performance of MgH_2. Metal-organic frameworks (MOFs) have been proven to be ideal precursors for the preparation of metal sulfides [39]. MOF derived sulfides can be obtained by calcination in different atmospheres (such as air, H_2, and Ar) and are more stable and conductive than primal MOFs [40]. In addition to retaining the original composition and characteristics of MOFs, MOF derived materials possess larger specific surface area and higher porosity and even hold better catalytic effect than primal MOFs [41].

It is noteworthy that bimetal and MOF derived sulfides are promising candidates for MgH_2 hydrogen storage system. In a recent research, Zhang *et al.* designed defect-rich $Ni_{0.67}Fe_{0.33}$−MOF by a solvothermal method, providing more options for efficient OER systems [42]. Stimulated by the pioneering achievements, we synthesized NiFe-MOF and firstly designed $FeNi_3$-S successfully to reveal whether NiFe-MOF and $FeNi_3$-S could promote hydrogen absorption and desorption properties of Mg/MgH_2 system. Through a systematic study of the de/resorption behavior of $FeNi_3$-S doped MgH_2 composites, we have demonstrated that $FeNi_3$-S imparted a notable improvement to the hydrogen storage properties of MgH_2. With the aid of structural and morphological characterizations, the synergistic catalytic mechanism of $FeNi_3$-S was discussed in detail.

NiFe-MOFs were prepared by a reported solvothermal method [42] with a slight modification. Thiophene-2,5-dicarboxylic acid (H_2TDC, Macklin, 98 %) and *N*,*N*-dimethylformamide (DMF, Macklim AR) were selected as organic ligand and solvent, while $Ni(NO_3)_2\cdot 6H_2O$ (Alfa Aesar, 98 %) and $Fe(NO_3)_3\cdot 9H_2O$ (Sinopharm Chemical Reagent Co., Ltd., AR) were used as nickel and iron sources. None of the chemicals used were further purified. The preparation process was as follows. 4 mmol $Ni(NO_3)_2\cdot 6H_2O$, 4 mmol $Fe(NO_3)_3\cdot 9H_2O$ and 5 mmol H_2TDC were added into a mixture of 60 mL DMF and deionized water. After complete dissolution, the blended solution was heated at 120 °C in a 100 mL Teflon-lined autoclave for 12 h. The sediment was collected by centrifugation, which was washed more than five times with a mixed 1:1 ratio of deionized water and ethanol solution to remove residual reactants. After a 12 h vacuum-drying period, the resulting brownish-yellow product was named as NiFe-MOF. The NiFe-MOF was then calcined at 400 °C for 2.5 h under a 4 MPa H_2 atmosphere to obtain $FeNi_3$-S.

MgH_2 was synthesized from commercially available Mg (Aladdin, purity 99.99 %, 100–200 mesh) in our laboratory *via* several times of ball-milling and hydrogenation. Mg was hydrogenated at 380 °C under 7 MPa H_2 pressure for 3 h. The samples were transferred into a stainless mill pot (Nanjing Chishun, 40:1 ball-to-powder weight ratio) and milled at a speed of 450 rpm for 5 h. After repeating the above steps twice, MgH_2 powder was successfully fabricated. 100 mg NiFe-MOFs and 100 mg $FeNi_3$-S were added into 900 mg as-prepared MgH_2 powder respectively by ball milling at a speed of 400 rpm for 6 h. All operations were conducted in an argon-fille glovebox (MIKROUNA), where H_2O and O_2 levels all below 0.1 ppm.

The phase compositions of the samples were undertaken *via* X-ray diffraction (Smart Lab SE 6 kW) tests, scanning from 20° to 80° at a rate of 6°/min. The micromorphology of the sample was characterized by scanning electron microscope (SEM, Hitachi SU8600) and transmission electron microscopy (TEM, JEM-2100F). The corresponding energy dispersive X-ray spectroscopy (EDS) displayed the element distribution. A Pressure-Composition-Temperature (PCT) equipment had been self-established to research the hydrogen storage properties (more detailed explanation could be found in the supporting information). Before each experiment, 120–150 mg powders were transferred into a steel tube, which was specially designed for hydrogen storage performance tests in our lab. The non-isothermal dehydrogenation was conducted at a heating rate of 5 °C/min from room temperature to 450 °C, while the non-isothermal hydrogen absorption was 1 °C/min. In isothermal experiments, the samples were performed at constant temperatures. The initial hydrogen pressure of absorption was 3.2 MPa, and that of dehydrogenation was lower than 0.001 MPa. For cyclic experiments, the composite was similarly hydrogenated at 3.0 MPa, dehydrogenated at 0.001 MPa, and repeated 20 times at 300 °C.

The NiFe-MOF was synthesized *via* a self-assembly process under 120 °C for 12 h. The $FeNi_3$-S materials were then fabricated by calcinating NiFe-MOF at 400 °C for 2.5 h under the H_2 atmosphere. Fig. 1a shows the schematic diagram for the synthesis of the NiFe-MOF and $FeNi_3$-S materials.

The phase compositions of NiFe-MOF and $FeNi_3$-S were detected *via* XRD analysis. The XRD pattern of NiFe-MOF (Fig. S1 in

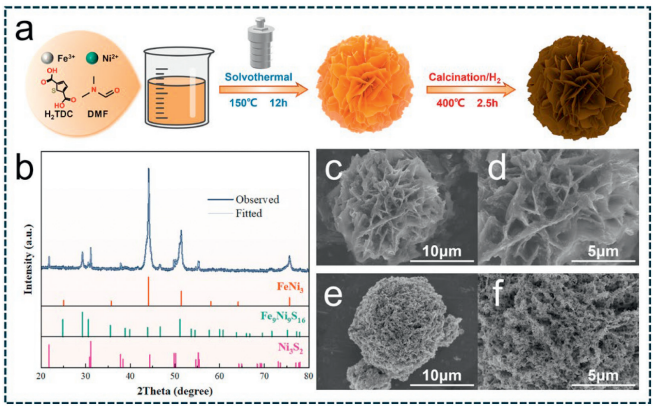


Fig. 1. (a) The schematic diagram for the synthesis process of NiFe-MOF and $FeNi_3$-S. (b) The XRD pattern of $FeNi_3$-S. (c, d) SEM patterns of NiFe-MOF. (e, f) SEM patterns of $FeNi_3$-S.

Supporting information) matched well with the previous research of Zhang *et al.* [42], which implied successful synthesis of NiFe-MOF. The XRD spectrum of $FeNi_3$-S was provided in Fig. 1b. Several sharp diffraction peaks could be perceived, indicating that the resultant $FeNi_3$-S had a good crystal structure. Three distinct diffraction peaks located at approximately 44.07°, 51.34°, and 75.56° were consistent with the characteristic peaks of $FeNi_3$. In addition to the prominent peaks corresponding to $FeNi_3$, the XRD pattern also exhibited minor peaks indicative of the presence of $Fe_9Ni_9S_{16}$ and Ni_3S_2, further describing the composition of the sample. The XRD result confirmed the formation of a multi-phase catalytic system consisting of $FeNi_3$ alloys and two mental sulfides (Ni_3S_2 and $Fe_9Ni_9S_{16}$). Thus, the hydrogen-annealed NiFe-MOF was labeled as $FeNi_3$-S in this work.

Morphological and structural analysis of the NiFe-MOF and $FeNi_3$-S material were carried out through SEM. Micron-sized NiFe-MOF (Figs. 1c and d) was corroborated as a nanoflower morphology and consisted of many petal-like nanosheets. The average thickness of these petal-like nanosheets was 20 nm. The magnified image is shown in the Figs. S2a and b (Supporting information). These nanosheets possessed uneven surface with many small particles decorated on it. After calcination, the matrix shape of the MOF did not collapse as shown in Figs. 1e and f. $FeNi_3$-S had a nanoflower structure as well, with a host of macropores and mesopores formed on the petal-like surface. The nanosheets transformed into many irregular nanopores and nanoparticles (Figs. S2c and d in Supporting information). The shapes of these nanoparticles were primarily linear, with an average width of 0.041 μm. Additionally, larger flake-like particles and finer particles could also be observed. Irregular shapes and pores provided a larger specific surface area and shorter diffusion channels, endowing $FeNi_3$-S with higher catalytic activity.

To compare the catalytic effect of the as-synthesized NiFe-MOF and $FeNi_3$-S, non-isothermal dehydrogenation tests were implemented on pure MgH_2, $MgH_2 + 10$ wt% NiFe-MOF composite and $MgH_2 + 10$ wt% $FeNi_3$-S composite. The non-isothermal dehydrogenation processes were shown in Fig. 2a. Obviously, the doping of the NiFe-MOF and $FeNi_3$-S catalyst significantly reduced the initial desorption temperature of MgH_2. Pure MgH_2 began to dehydrogenate at a high temperature of 325 °C. The initial dehydrogenation temperature of NiFe-MOF dopped MgH_2 was decreased to 227 °C, while that of $FeNi_3$-S modified MgH_2 was further shifted to 202 °C. The corresponding differential curves compared the peak dehydrogenation temperature of MgH_2 dopped with NiFe-MOF and $FeNi_3$-S. Specifically, $MgH_2 + 10$ wt% $FeNi_3$-S composite exhibited a peak dehydrogenation temperature of 307 °C, while $MgH_2 + 10$ wt%

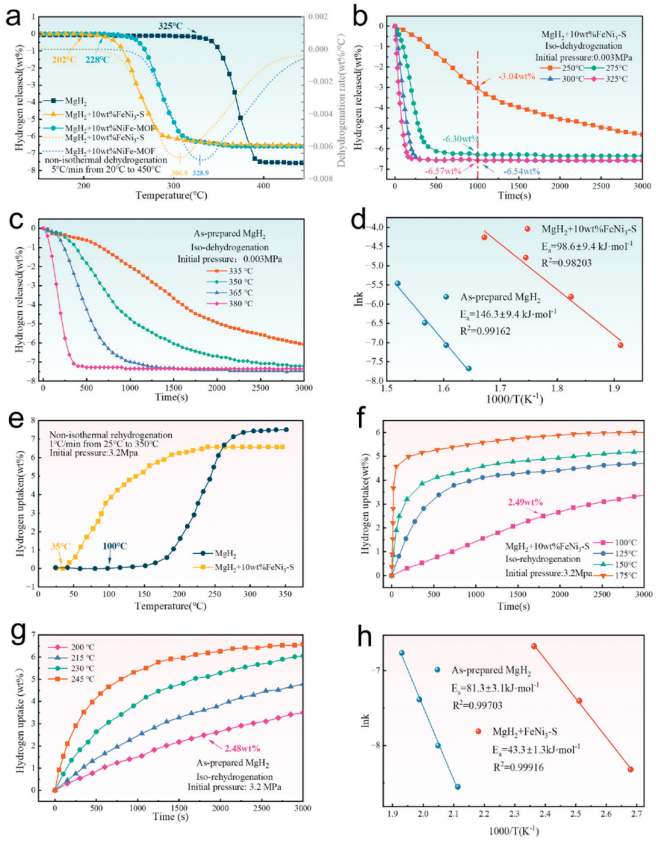


Fig. 2. (a) Non-isothermal dehydrogenation curves of $MgH_2 + 10$ wt% (NiFe-MOF/$FeNi_3$-S) composites and the corresponding differential curves. (b) Isothermal dehydrogenation curves of $MgH_2 + 10$ wt% $FeNi_3$-S composites at 250, 275, 300 and 325 °C. (c) Isothermal dehydrogenation curves of MgH_2 at 335, 350, 365 and 380 °C. (d) Fitted Arrhenius curves of MgH_2 and $MgH_2 + 10$ wt% $FeNi_3$-S composites. (e) Non-isothermal hydrogenation curves of $MgH_2 + 10$ wt% (NiFe-MOF/$FeNi_3$-S) composites. (f) Isothermal hydrogenation curves of $MgH_2 + 10$ wt% $FeNi_3$-S composites at 100, 125, 150 and 175 °C. (g) Isothermal hydrogenation curves of MgH_2 at 200, 215, 230 and 245 °C. (h) Fitted Arrhenius curves of MgH_2 and $MgH_2 + 10$ wt% $FeNi_3$-S composites.

$FeNi_3$-S composite showed a peak dehydrogenation temperature of 329 °C.

The results above revealed that NiFe-MOF and $FeNi_3$-S both had splendid influences on hydrogen desorption process of MgH_2. Between the two doped systems, $MgH_2 + 10$ wt% $FeNi_3$-S composite exhibited superior dehydrogenation properties. Therefore, $MgH_2 + 10$ wt% $FeNi_3$-S composite was selected for subsequent kinetic investigations. It could also be observed from the curves that the hydrogen storage capacity inevitably decreased with the addition of the catalyst due to lower proportion of MgH_2 in the composite. One the other hand, combined with sulfides in $FeNi_3$-S, a small amount of Mg had been converted to MgS. This would be explained in detail in subsequent sections.

Fig. 2b displays the isothermal hydrogen desorption kinetic curves of the $MgH_2 + 10$ wt% $FeNi_3$-S composite at 250, 275, 300, and 325 °C. Consistent with expectations, the desorption process performed swifter kinetics upon the elevation of the temperature. At 325 °C, $MgH_2 + 10$ wt% $FeNi_3$-S composite could release 6.57 wt% H_2 (fully dehydrogenated) within 1000 s. When the temperature reached 275 °C, $MgH_2 + 10$ wt% $FeNi_3$-S composite still quickly liberated 6.30 wt% H_2 within 1000 s. Furthermore, it was noted that at the comparatively lower temperature of 250 °C, the same material was capable to desorb 3.04 wt% H_2 within 1000 s. In the control experiments, as-prepared MgH_2 exhibited a quite sluggish dehydriding rate (Fig. 2c). Undoped-MgH_2 could only release 2.0

wt% H_2 within 1000 s even at a high temperature of 335 °C, which was 1.0 wt% less than $MgH_2 + 10$ wt% $FeNi_3$-S composite at a lower temperature of 250 °C.

To delve deeper into the effect of $FeNi_3$-S on the dehydriding reaction of MgH_2, the apparent activation energy (E_a) for dehydrogenation was computed utilizing both the Johnson-Mehl-Avrami-Kolmogorov (JMAK) model and the Arrhenius equation. The formulation of the JMAK model was as follows:

$$\ln\left[-\ln(1-\alpha)\right] = n\ln k + \ln t \quad (1)$$

where α was the extent of the reaction, t denoted the reaction duration, n denoted the Avrami exponent, and k represented the rate constant. Thereafter, E_a was ensured using the Arrhenius equation:

$$k = A\exp\left(-\frac{E_a}{RT}\right) \quad (2)$$

where k denoted the rate constant, T meant the isothermal hydrogen desorption temperature, A and R represented the pre-exponential factor and the gas constant respectively. In this work, the calculated values of E_a (Fig. 2d) in dehydrogenation reaction for $MgH_2 + 10$ wt% $FeNi_3$-S composite was 98.6 kJ/mol, achieving a 33 % reduction compared to that of pure MgH_2 (146.3 kJ/mol). Manifestly, the incorporation of $FeNi_3$-S nanoflowers significantly diminished the reaction barrier in the dehydrogenation process, thereby greatly enhancing the dehydrogenation kinetics of MgH_2.

To analyze the performance of hydrogen absorption, non-isothermal and isothermal hydrogenation experiments were conducted for as-prepared MgH_2 and $MgH_2 + 10$ wt% $FeNi_3$-S composite. Fig. 2e compares the non-isothermal hydrogen absorption results for as-prepared MgH_2 and $MgH_2 + 10$ wt% $FeNi_3$-S composite. Evidently, the addition of the catalyst facilitated a substantial improvement in hydrogen absorption properties. The initial hydrogenation temperature of MgH_2 was approximate 100 °C. Noteworthy, the introduction of $FeNi_3$-S resulted in a remarkable decrease to 35 °C, which was 65 °C lower than the as-prepared MgH_2. Fig. 2f presents the isothermal hydrogen absorption kinetic curves of the $MgH_2 + 10$ wt% $FeNi_3$-S composite at 100, 125, 150, and 175 °C. It can be observed that the $MgH_2 + 10$ wt% $FeNi_3$-S composite reabsorbed 2.49 wt% H_2 at 100 °C within 30 min. This was in stark contrast to MgH_2 (Fig. 2g), which necessitated a significantly higher temperature of 200 °C to release an equivalent mass of hydrogen under identical experimental conditions. The above data illustrated that $FeNi_3$-S doped MgH_2 displayed superior hydrogen storage capability at low temperatures, along with rapid hydrogen absorption kinetics. To gain more profound understanding of the hydrogenation kinetics, E_a was calculated by using the JMAK model Eq. 1 and Arrhenius equation Eq. 2. Only 100, 125, and 150 °C were selected to calculate the activation energy since the rate of hydrogen absorption at 175 °C was excessively fast, which would result in a poor goodness of fit. As shown in Fig. 2h, the doping of $FeNi_3$-S lowered the E_a value for hydrogen absorption of MgH_2 from 81.3 kJ/mol to 43.3 kJ/mol, affirming the outstanding hydrogen absorption property of $MgH_2 + 10$ wt% $FeNi_3$-S composite.

The outstanding catalytic effect of $FeNi_3$-S in the first de/absorption cycle prompted in-depth research on the cycling stability of $FeNi_3$-S doped MgH_2 composite, which was a critical indicator for the commercial viability of MgH_2. Fig. 3a details the fluctuations in hydrogen storage capacity and presents several typical cycles over the first 20 isothermal consecutive dehydrogenation and hydrogenation cycles. After 20 cycles, the $MgH_2 + 10$ wt% $FeNi_3$-S composite maintained desorption and absorption content at 6.2 wt% and 6.3 wt%, and the retention ratio was 94.2 % and 96.0 % respectively. In addition, the curves depicted that the $MgH_2 + 10$ wt% $FeNi_3$-S composite was able to complete hydrogen release and uptake reaction within 10 min during all the 20 cycles.

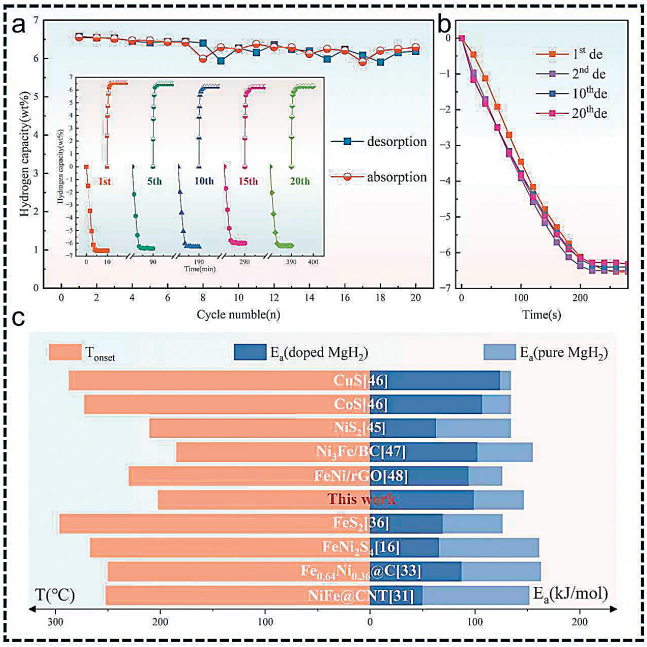


Fig. 3. (a) Dehydrogenation and rehydrogenation cycles of $MgH_2 + 10$ wt% $FeNi_3$-S composites at 300 °C (the inset figure is representative dehydrogenation and rehydrogenation cycles). (b) Comparisons of different dehydrogenation curves during the 20 cycles. (c) Current studies on FeNi alloy and FeNi sulfide catalysts for MgH_2 [16,31,33,36,45–48].

In conclusion, the $MgH_2 + 10$ wt% $FeNi_3$-S composite manifested an exceptional cycling performance with stable retention both in capacity and kinetics, indicating that $FeNi_3$-S served as a highly potent and reliable catalyst for MgH_2 to enhance the cycling life of MgH_2. Notably, the hydrogen capacity of the composite exhibited a slight decrease but then rebounded, potentially attributed to the formation and decomposition of magnesium oxide layer on MgH_2/Mg [43]. In addition, it was observed that the kinetics of dehydrogenation improved from the first cycle to the latter (Fig. 3b), which had been studied in our former studies [44]. After several cycle activation, $MgH_2 + 10$ wt% $FeNi_3$-S composite was activated, making it more amenable to hydrogen de/absorption. The $FeNi_3$, Fe and MgS generated during the activation could significantly improve the kinetics of MgH_2. Analyses suggested that the $MgH_2 + 10$ wt% $FeNi_3$-S composite was supposed to undergo several activation cycles to improve its initial hydrogen storage performance and to ensure its reliability and stability for long-term use.

Based on the discussion of experimental results and theoretical calculation, it was reasonable to conclude that $FeNi_3$-S efficiently modified the kinetic and thermodynamic properties of MgH_2. Fig. 3c compiled some current studies on FeNi alloy and FeNi sulfide added in MgH_2, which provided solid evidence for the superior hydrogen storage performances of the $MgH_2 + 10$ wt% $FeNi_3$-S composite [16,31,33,36,45–48].

To comprehensively elucidate the catalytic mechanism of $FeNi_3$-S, relevant characterizations were conducted to ascertain the phase composition and microstructure of $MgH_2 + 10$ wt% $FeNi_3$-S composite under diverse states. Fig. 4a is the XRD spectrum of the $MgH_2 + 10$ wt% $FeNi_3$-S composite after ball milling, hydrogenation, dehydrogenation and 20 cycles. Diffraction peaks of MgH_2 and $FeNi_3$-S were detected in the ball milled state, but other phases of $FeNi_3$-S were almost undetectable due to their low concentration. It suggested that no chemical transformation occurred during the ball milling process. The observed broadening of the XRD peaks implied that the crystallite size of MgH_2 and $FeNi_3$-S had been significantly reduced after ball milling. Mg and MgH_2

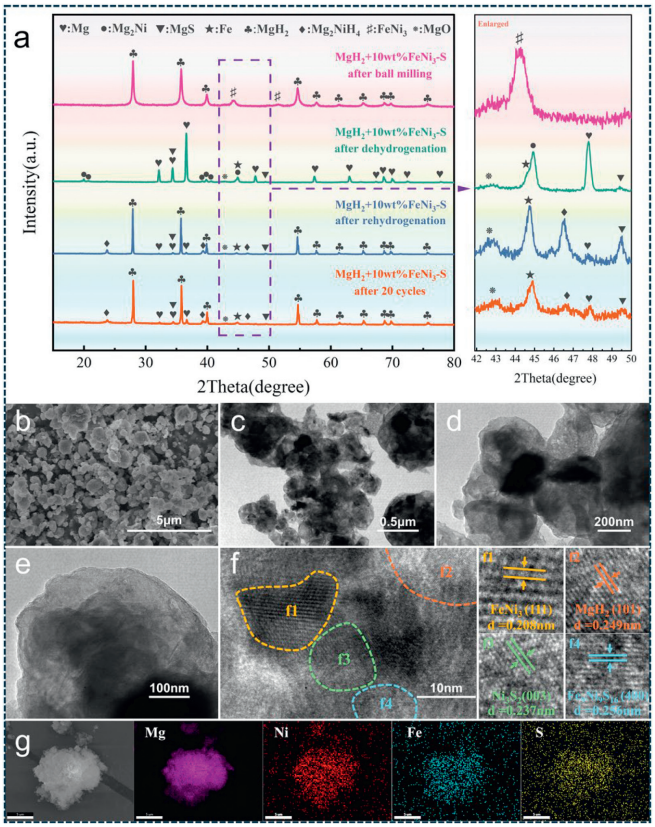


Fig. 4. (a) The XRD patterns of $MgH_2 + 10$ wt% $FeNi_3$-S composites after ball-milling, de/rehydrogenation and 20 cycles. (b) SEM pattern of the $MgH_2 + 10$ wt% $FeNi_3$-S composite. (c–e) TEM patterns of $MgH_2 + 10$ wt% $FeNi_3$-S composites. (f) HRTEM patterns of the $MgH_2 + 10$ wt% $FeNi_3$-S composite. (g) EDS mapping of the $MgH_2 + 10$ wt% $FeNi_3$-S composite.

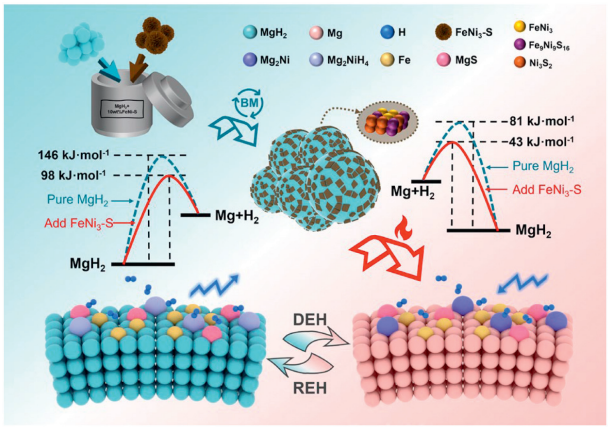


Fig. 5. Schematic illustration of multi-phase synergistic catalytic mechanism of the $MgH_2 + 10$ wt% $FeNi_3$-S composite.

were the main phase in de/re-hydrogenated states respectively. After dehydrogenation, $FeNi_3$-S had been decomposed. MgH_2 was converted into Mg, along with the *in-situ* emergence of several new phases including Mg_2Ni, MgS, and Fe. The phase transformation of $MgH_2 + 10$ wt% $FeNi_3$-S composite in dehydrogenation could be outlined below:

$$MgH_2 \rightarrow Mg + H_2 \quad (3)$$

$$8MgH_2 + Ni_3S_2 \rightarrow 2MgS + 3Mg_2Ni + 8H_2 \quad (4)$$

$$34MgH_2 + Fe_9Ni_9S_{16} \rightarrow 16MgS + 9Mg_2Ni + 9Fe + 34H_2 \quad (5)$$

Compared with the ball-milled state, the XRD patterns of the $MgH_2 + 10$ wt% $FeNi_3$-S composite exhibited increased intensity and sharpness after de/re-hydrogenation. This enhancement could be attributed to the disappearance of lattice distortions and crystal defects, which were initially introduced during the ball milling process and subsequently mitigated during heating and hydrogenation [45]. The existence of Mg phase in rehydrogenated state was probably due to the partial hydrogenation caused by insufficient hydriding time. After 20 cycles, the feature diffraction peaks of Mg_2NiH_4, MgS and Fe were observed. Additionally, the diffraction peaks located at approximately 43° and 62° belonged to MgO. The formation of MgO was potentially attributable to the reaction between Mg particles and residual oxygen that was unavoidably introduced into the system during 20 cycles. Fortunately, the surface oxide layer gradually disintegrated with the ongoing cycling [43], contributing to the recovery of hydrogen storage capacity which correlated with the observed trend in hydrogen capacity curve (Fig. 3a). Characteristic peaks for Mg were also observed. This could be attributed to that Mg particles were prone to agglomeration and growth in the continuous cycles of hydrogenation and dehydrogenation [21], which led to the internal Mg being unable to react with H_2 and form MgH_2. Thus, the hydrogen content gradually declined as the cycles progress.

SEM, TEM, HRTEM and EDS mapping were carried out to further discover the microstructure of ball-milled $MgH_2 + 10$ wt% $FeNi_3$-S composite. After ball milling, the MgH_2 and $FeNi_3$-S were ground into many irregular fragments that were stacked upon one another (Fig. 4b). Figs. 4c–e depicted that $FeNi_3$-S particles were inlaid on the surface of MgH_2. Both MgH_2 and $FeNi_3$-S particles exhibited a relatively small size. HRTEM patterns in Fig. 4f confirmed the existence of MgH_2 (101), $FeNi_3$ (111), Ni_3S_2 (003) and $Fe_9Ni_9S_{16}$ (400) planes according to the lattice fringe spacings. As a supplementary argument to the XRD pattern, HRTEM images reaffirmed that $FeNi_3$-S did not undergo any chemical transformation during the ball milling process. Different phases of $FeNi_3$-S intimately connected thus offering a multitude of boundaries and interfaces. EDS mapping images (Fig. 4g) revealed a uniform distribution of nickel, iron, and sulfur elements throughout the material. The uniform distribution of $FeNi_3$-S stemmed from the unique carbon skeleton inherited from NiFe-MOF.

Based on the characterization results presented above, the catalytic mechanism can be summarized as follows (Fig. 5): (1) $FeNi_3$-S was a MOF derived multi-phase catalyst composed of nickel-iron alloy and nickel-iron sulfide. The special nanoflower morphology, replete with an array of irregular nanopores, was instrumental in facilitating shorter diffusion pathways and the exposure of numerous active sites. This intricate architecture endowed $FeNi_3$-S with remarkable catalytic performance. (2) After ball milling, the nanoflower-like structure fragmented into a variety of nanoparticle, homogeneously dispersing across the surface of MgH_2. During the heating and the first dehydrogenation, $FeNi_3$-S reacted with MgH_2 and formed multi-phase catalysts in suit. Henceforth, the $Mg/Mg_2Ni + Fe/MgS$ and $MgH_2/Mg_2NiH_4 + Fe/MgS$ hydrogen storage systems had been successfully developed. The multifaceted interface facilitated the dissociation and recombination of H molecules by offering expanded active sites and diffusion pathways, thus improving the de/rehydrogenation properties of MgH_2/Mg. Our recent research had proven that the enthalpy of formation for the Mg_2Ni/Mg_2NiH_4 was lower than that of the Mg/MgH_2 [49]. Hence, Mg_2Ni/Mg_2NiH_4 altered the original reaction pathway, reducing the theoretical energy required for hydrogen desorption and absorption. In brief, Mg_2Ni/Mg_2NiH_4 could

de/absorb hydrogen more easily and rapidly than the Mg/MgH_2 system, which had been previously studied and was referred to as "hydrogen pump" [19,20]. Besides, both Fe and MgS were consistently stable within the reaction system, functioning effectively as "hydrogen diffusion channel" to expedite hydrogen migration. Interestingly, Zhang *et al.* had experimentally verified that the co-catalytic impacts of Fe and MgS outperformed the individual catalytic effect when Fe or MgS was added separately [37]. Thereby, the synergistic catalytic effect of Mg_2Ni/Mg_2NiH_4, along with Fe and MgS markedly boosted the hydrogen storage properties of Mg/MgH_2 system. (3) The carbon skeleton, inherited from NiFe-MOF to $FeNi_3$-S, played a pivotal role in preventing the agglomeration and growth of MgH_2 throughout the cyclic processes, thereby effectively improving the cycle performance.

In this study, MOF-derived nanoflower-like $FeNi_3$-S was successfully designed by the process of solvothermal and calcination, which was proven effective in improving the hydrogen storage properties of MgH_2. The initial dehydrogenation temperature of $MgH_2 + 10$ wt% $FeNi_3$-S composite was 202 °C, which was 123 °C lower than that of MgH_2. At 250 °C and 325 °C, $MgH_2 + 10$ wt% $FeNi_3$-S released 3.04 wt% H_2 and 6.57 wt% H_2 (fully dehydrogenated) within 1000 s. Surprisingly, $MgH_2 + 10$ wt% $FeNi_3$-S composite began to rehydrogenate at room temperature and rapidly absorb 2.49 wt% H_2 within 30 min at 100 °C. Based on the activation energy fitting calculations, the addition of $FeNi_3$-S enhanced the de/resorption kinetics of MgH_2 at low temperatures ($E_a = 98.6$ kJ/mol and 43.3 kJ/mol respectively). Furthermore, multi-phase synergistic catalytic effect was further proposed. The fast kinetics at low temperatures of $MgH_2 + 10$ wt% $FeNi_3$-S composite was owning to the *in-situ* formed $Mg/Mg_2Ni + Fe/MgS$ and $MgH_2/Mg_2NiH_4 + Fe/MgS$ hydrogen storage systems. The multi-phase synergistic catalytic effect between hydrogen pump (Mg_2Ni/Mg_2NiH_4) and active sites provided by Fe/MgS greatly improved the hydrogen storage property of MgH_2. In a summary, the combination between transition metal alloys (TMAs) and transition metal sulfides (TMSs) showed impressive catalytic effect on the de/resorption processes of MgH_2, which opened up new avenues and provided fresh insights into overcoming the obstacles in Mg-based hydrogen storage. The results of the study were also useful for predicting the products of MOFs after calcination.

Declaration of competing interest

The authors declare that they have no known competing financial interests or personal relationships that could have appeared to influence the work reported in this paper.

CRediT authorship contribution statement

Linxin Zheng: Writing – original draft, Investigation. **Shuai Li:** Writing – original draft, Methodology. **Liuting Zhang:** Writing – review & editing. **Tao Zhong:** Validation, Formal analysis. **Xiuzhen Wang:** Supervision, Funding acquisition. **Ting Bian:** Funding acquisition. **Petr Senin:** Supervision. **Ying Wu:** Supervision, Funding acquisition.

Acknowledgments

This work was supported by the National Key R&D Program of China (No. 2022YFB3803703), the National Natural Science Foundation of China (Nos. 52071141, 52271212, 52201250, 51771056, 22305104), the Natural Science Foundation of Jiangsu Province (No. BK20210893) and the Ministry of Science and Technology of the People's Republic of China (No. G2023014022L).

Supplementary materials

Supplementary material associated with this article can be found, in the online version, at doi:10.1016/j.cclet.2024.110414.

References

[1] J.O. Abe, A.P.I. Popoola, E. Ajenifuja, et al., Int. J. Hydrog. Energy 44 (2019) 15072–15086.
[2] M.R. Usman, Renew. Sustain. Energy Rev. 167 (2022) 112743.
[3] E.H. Abdechafik, H.A. Ousaleh, S. Mehmood, et al., Int. J. Hydrog. Energy 52 (2024) 1182–1193.
[4] O. Faye, J. Szpunar, U. Eduok, Int. J. Hydrog. Energy 47 (2022) 13771–13802.
[5] Y. Wang, Y. Xue, A. Züttel, Chem. Soc. Rev. 53 (2024) 972–1003.
[6] X. Zhang, Y. Liu, X. Zhang, et al., Mater. Today Nano 9 (2020) 100064.
[7] L. Ren, Y. Li, N. Zhang, et al., Nano Micro Lett. 15 (2023) 93.
[8] C. Zhou, Y. Peng, Q. Zhang, J. Mater. Sci. Technol. 50 (2020) 178–183.
[9] Y. Shang, C. Pistidda, G. Gizer, et al., J. Magn. Alloy. 9 (2021) 1837–1860.
[10] V.V. Berezovets, R.V. Denys, I.Y. Zavaliy, et al., Int. J. Hydrog. Energy 47 (2022) 7289–7298.
[11] Y. Zhang, G. Wu, J. Gu, et al., Rare Met. 43 (2024) 3260–3272.
[12] J. Zhang, X. Ding, R. Chen, et al., J. Power Sources 548 (2022) 232037.
[13] Y. Fu, Z. Ding, S. Ren, et al., Int. J. Hydrog. Energy 45 (2020) 28154–28162.
[14] H. Huang, T. Xu, J. Chen, et al., Chem. Eng. J. 483 (2024) 149434.
[15] S. Li, L. Zhang, F. Wu, et al., Chin. Chem. Lett. 36 (2025) 109566.
[16] Y. Fu, L. Zhang, Y. Li, et al., J. Magn. Alloys. 11 (2023) 2927–2938.
[17] X. Xie, B. Zhang, H. Kimura, et al., Chem. Eng. J. 464 (2023) 142630.
[18] N.S. Norberg, T.S. Arthur, S.J. Fredrick, et al., J. Am. Chem. Soc. 133 (2011) 10679–10681.
[19] X. Li, Y. Fu, Y. Xie, et al., Int. J. Hydrog. Energy 46 (2021) 33186–33196.
[20] X. Yang, Q. Hou, L. Yu, et al., Dalton Trans. 50 (2021) 1797–1807.
[21] M. Song, L. Zhang, Z. Yao, et al., Inorg. Chem. Front. 9 (2022) 3874–3884.
[22] P.K. Soni, A. Bhatnagar, M.A. Shaz, Int. J. Hydrogen Energy 48 (2023) 17970–17982.
[23] D. Pukazhselvan, N. Nasani, P. Correia, et al., J. Power Sources 362 (2017) 174–183.
[24] D. Pukazhselvan, K.S. Sandhya, D. Ramasamy, et al., ChemPhysChem 21 (2020) 1195–1201.
[25] B. Liu, B. Zhang, X. Chen, et al., Mater. Today Nano 17 (2022) 100168.
[26] L. Li, G. Jiang, H. Tian, et al., Int. J. Hydrog. Energy 42 (2017) 28464–28472.
[27] Y. Meng, J. Zhang, S. Ju, et al., J. Mater. Chem. A 11 (2023) 9762–9771.
[28] Z. Wang, Z. Ren, N. Jian, et al., J. Mater. Chem. A 6 (2018) 16177–16185.
[29] S. Guo, Z. Yu, Y. Li, et al., J. Alloy. Compd. 976 (2024) 173035.
[30] L. Zhang, H. Yu, Z. Lu, et al., Chin. J. Chem. Eng. 43 (2022) 343–352.
[31] Y. Fu, Z. Yu, S. Guo, et al., Chem. Eng. J. 458 (2023) 141337.
[32] M. Pozzo, D. Alfè, Int. J. Hydrog. Energy 34 (2009) 1922–1930.
[33] Z. Ding, Y. Fu, L. Zhang, et al., J. Alloy. Compd. 843 (2020) 156035.
[34] W. He, F. Wang, Y. Gao, et al., Sustain. Energy Fuels 6 (2022) 3852–3857.
[35] J. Mei, Y. Deng, X. Cheng, et al., Chin. Chem. Lett. 35 (2024) 108900.
[36] W. Zhang, G. Xu, Y. Cheng, et al., Dalton Trans. 47 (2018) 5217–5225.
[37] W. Zhang, Y. Cheng, D. Han, et al., Energy 93 (2015) 625–630.
[38] L. Zeng, Z. Lan, B. Li, et al., J. Magn. Alloy. 10 (2022) 3628–3640.
[39] D. Zhou, K. Cui, Z. Zhou, et al., Int. J. Hydrog. Energy 46 (2021) 34369–34380.
[40] Y. Qian, F. Zhang, S. Zhao, et al., Nano Energy 111 (2023) 108415.
[41] Y. Chen, R. Zhang, L. Jiao, et al., Coord. Chem. Rev. 362 (2018) 1–23.
[42] S. Zhang, Z. Huang, T.T. Isimjan, et al., Appl. Catal. B: Environ. 343 (2024) 123448.
[43] L. Ren, Y. Li, Z. Li, et al., Nano Micro Lett. 16 (2024) 160.
[44] L. Zhang, L. Ji, Z. Yao, et al., Int. J. Hydrog. Energy 44 (2019) 21955–21964.
[45] P. Wang, Z. Wang, Z. Tian, et al., Renew. Energy 160 (2020) 409–417.
[46] P. Wang, Z. Tian, Z. Wang, et al., Int. J. Hydrog. Energy 46 (2021) 27107–27118.
[47] Q. Hou, J. Zhang, Z. Zheng, et al., Dalton Trans. 51 (2022) 14960–14969.
[48] L. Ji, L. Zhang, X. Yang, et al., Dalton Trans. 49 (2020) 4146–4154.
[49] T. Zhong, T. Xu, L. Zhang, et al., J. Magn. Alloy. 13 (2025) 148–160.